
This is an electronic reprint of the original article.
This reprint may differ from the original in pagination and typographic detail.

Heilmann, Rebecca; Arjas, Kristian; Hakala, Tommi K.; Törmä, Päivi
Multimode Lasing in Supercell Plasmonic Nanoparticle Arrays

Published in:
ACS Photonics

DOI:
[10.1021/acsp Photonics.3c00761](https://doi.org/10.1021/acsp Photonics.3c00761)

Published: 15/11/2023

Document Version
Publisher's PDF, also known as Version of record

Published under the following license:
CC BY

Please cite the original version:
Heilmann, R., Arjas, K., Hakala, T. K., & Törmä, P. (2023). Multimode Lasing in Supercell Plasmonic Nanoparticle Arrays. *ACS Photonics*, 10(11), 3955-3962. <https://doi.org/10.1021/acsp Photonics.3c00761>

This material is protected by copyright and other intellectual property rights, and duplication or sale of all or part of any of the repository collections is not permitted, except that material may be duplicated by you for your research use or educational purposes in electronic or print form. You must obtain permission for any other use. Electronic or print copies may not be offered, whether for sale or otherwise to anyone who is not an authorised user.

Multimode Lasing in Supercell Plasmonic Nanoparticle Arrays

Published as part of the ACS Photonics virtual special issue "Frontiers and Applications of Plasmonics and Nanophotonics".

Rebecca Heilmann, Kristian Arjas, Tommi K. Hakala, and Päivi Törmä*



Cite This: *ACS Photonics* 2023, 10, 3955–3962



Read Online

ACCESS |



Metrics & More



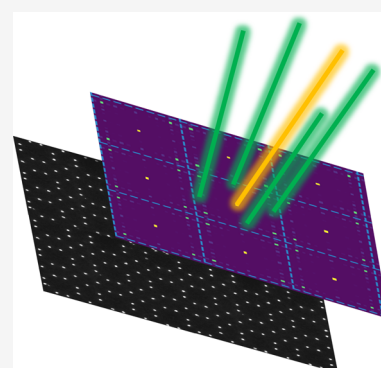
Article Recommendations



Supporting Information

ABSTRACT: Multicolor light sources can be used in applications such as lighting and multiplexing signals. In photonic and plasmonic systems, one way to achieve multicolor light is via multimode lasing. To achieve this, plasmonic nanoparticle arrays are typically arranged in superlattices that lead to multiple dispersions of the single arrays coupled via the Bragg superlattice Bragg modes. Here, we show an alternative way to enable multimode lasing in plasmonic nanoparticle arrays. We design a supercell in a square lattice by leaving part of the lattice sites empty. This results in multiple dispersive branches caused by the supercell period and hence creates additional band edges that can support lasing. We experimentally demonstrate multimode lasing in such a supercell array. Furthermore, we identify the lasing modes by calculating the dispersion by combining the structure factor of the array design with an empty lattice approximation. We conclude that the lasing modes are the 74th Γ - and 106th X -point of the supercell. By tuning the square lattice period with respect to the gain emission, we can control the modes that lase. Finally, we show that the lasing modes exhibit a combination of transverse electric and transverse magnetic mode characteristics in polarization-resolved measurements.

KEYWORDS: plasmonics, nanophotonics, surface plasmon resonance, multimode lasing



INTRODUCTION

Plasmonic nanoparticle arrays support surface lattice resonances (SLRs) that are dispersive plasmonic–photonic modes arising from a hybridization between the plasmonic resonances of individual nanoparticles and the diffracted orders governed by the lattice geometry. The spectral position of the SLRs can be easily tailored by varying the lattice geometry and period while simultaneously yielding high quality (Q-) factors.^{1–7} Combined with emitters such as organic dye molecules, plasmonic nanoparticle arrays are an effective system to study light–matter interactions such as strong coupling or Bose–Einstein condensation.^{8–13} Lasing in plasmonic nanoparticle arrays has been studied in various lattice geometries such as square, rectangular, honeycomb, or hexagonal lattices. Typically, the systems produce lasing at a band edge originating at high symmetry points of the lattice, for instance, at the Γ -, K -, or M -points.^{14–19} Also, bound states in continuum which have extraordinary high Q-factors have been recently exploited for lasing in plasmonic arrays.^{20–22}

For lighting applications and optical communication, multicolor light sources are necessary. Ideally, such sources span red, blue, and green wavelengths in order to create white light or NIR regions for optical communication.^{23–26} In photonic systems, one way to achieve multicolor light sources is via multimode lasing, i.e., simultaneous lasing at a set of different modes. As lasing occurs in plasmonic systems at band edges, multiple band

edges need to be created to realize multimode lasing. The most straightforward approach is by organizing individual arrays in a larger superlattice network, where the SLRs of the individual arrays couple to the Bragg modes of the superlattice, leading to multiple band edges at different energies and wavevectors.²⁷ Multimode lasing has been observed in such superlattice geometries.^{28,29} Another possibility to realize multimode lasing is by dividing a square array into smaller patches, which have slightly different periods. This creates additional band edges at different energies that simultaneously lase under optical pumping.³⁰

Another way of creating additional band edges for a zero wavevector, i.e., into the direction normal to the array plane, is by introducing an effective second lattice period which yields a second SLR. This can be done in bipartite arrays^{6,31,32} or by introducing periodic vacancies to the arrays.³³ By removing particles at designated positions, deterministic aperiodic lattices that yield more complicated band structures and hence

Received: June 6, 2023

Published: October 10, 2023



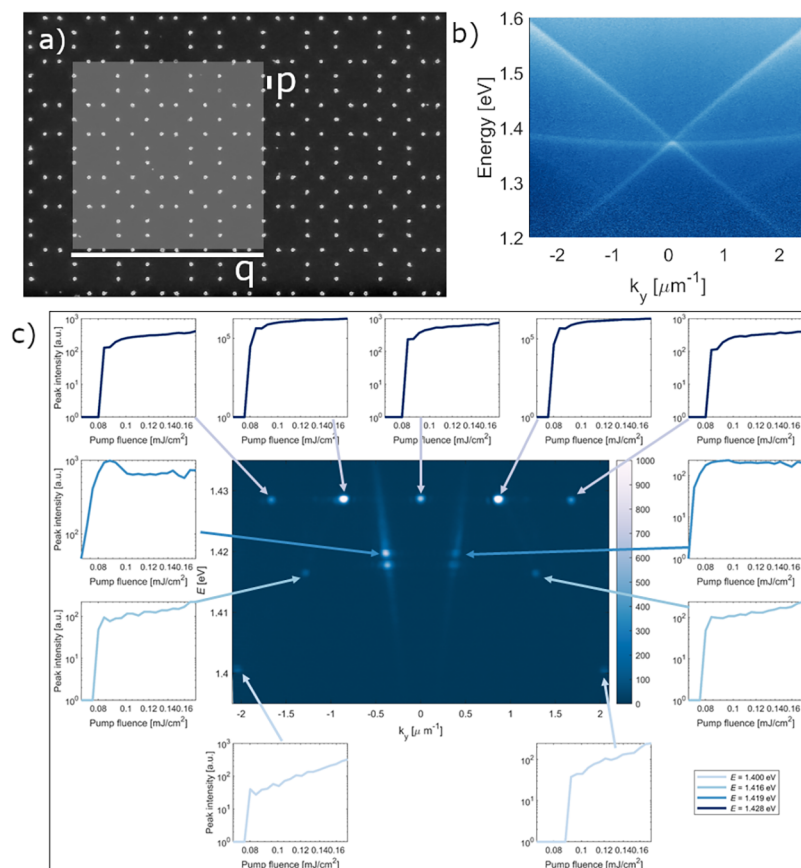


Figure 1. Lasing experiment in a supercell nanoparticle array. (a) SEM image of the array studied. The array is based on a square array structure (period $p = 596$ nm), where specific lattice sites are kept empty. The giant unit cell is highlighted (q is the unit cell size). (b) Measured transmission spectrum and (c) results of the lasing experiments. For the experiments in (c), the array is combined with organic dye molecules (IR 140, 10 mM). Multiple lasing peaks are visible at different energies and k_y (see central plot). The threshold behavior of the lasing peaks is shown as indicated by the arrows. The size of the supercell lattice is $115 \mu\text{m} \times 115 \mu\text{m}$.

additional band edges have been realized, and lasing in such lattices has been demonstrated.³⁴ However, multimode lasing has not been explicitly studied. Other systems in which multimode lasing has been observed include low-symmetry arrays, where two polarization-dependent modes lase simultaneously,³⁵ light-cone SLRs overlapping with higher Brillouin Zone (BZ) edges enabling lasing from several high symmetry points at once,³⁶ and lasing in quasi-propagating modes that span a continuum of energies.³⁷ In addition to the aforementioned plasmonic structures, multimode lasing has been achieved in various photonic systems such as hyperuniform structures,³⁸ topological insulators,^{39,40} bound states in the continuum,^{21,41} and as simultaneous lasing in the magnetic and electric resonances of a dielectric nanoparticle array.⁴²

Here we study lasing in a plasmonic square lattice, where we create a periodic supercell by removing particles at designated positions. We performed lasing experiments by combining the array with a solution of dye molecules. Under optical pumping, we observe multiple lasing peaks that emerge at different energies and nonzero wavevectors. To understand the interplay between the two periods in the system (underlying square and the supercell periods), we calculate the Empty Lattice Approximation (ELA) from the geometric structure factor and free photon dispersion.³⁴ We can see additional modes enabled by the much longer supercell period, which would otherwise be suppressed in the original square lattice. These new modes can be seen to exist at high-symmetry points of the Brillouin Zone

(BZ) as defined by the supercell: 74th Γ^- and 106th X-point if all possible modes are considered. While these modes are expected to exist in any square lattice matching the period of the supercell, by changing the positions of the particles in the unit cell, we can exhibit some control over the modes. This type of supercell and theoretical framework provide a new platform for designing multimode lasing systems.

EXPERIMENTS

We study a system based on a nanoparticle lattice with a square symmetry; however, part of the sites of the square array are left empty. This creates a unit cell of 13×13 sites, which is repeated over the whole array. In order to create the supercell lattice, we start with the supercell, i.e., a square array of a certain size. We then remove lattice sites such that a pattern is created, that is aperiodic. This aperiodic pattern is then repeated periodically. This is clearly different from, for instance, deterministic aperiodic arrays based on, e.g., the Fibonacci or Thue-Morse sequence. The size of the supercell lattice is $115 \mu\text{m} \times 115 \mu\text{m}$. An SEM image of the array is shown in Figure 1 a). Details of the sample fabrication and the measurement setup are given in the Supporting Information, including Figure S1. The period of the square array is $p = 596$ nm and hence, the period of the supercell is $q = 7748$ nm. The gold nanoparticles have a diameter of 120 nm and a height of 50 nm. A transmission measurement of the array is shown in Figure 1 b), where the dispersive surface lattice resonances (SLRs) are clearly visible. The SLRs correspond to

the underlying square array with the Γ -point located at $k_y = 0$, $E = 1.37$ eV. In transmission measurements, the finer features caused by the supercell are scarcely visible below the TM-branch.

We combine the nanoparticle array with a solution of organic dye molecules (IR 140, 10 mM) by sandwiching a droplet between the sample slide and a superstrate and pump the system optically with a left-circular polarized femtosecond laser (1 kHz repetition rate, 800 nm central wavelength). With increasing pump fluence, a set of narrow peaks emerge as shown in Figure 1c. The corresponding threshold curves, i.e., emission intensity versus pump fluence, are shown in the plots surrounding the spectrometer data recorded at a pump fluence of 0.1329 mJ/cm². At the highest energy of 1.428 eV there are five peaks at $k_y = -1.662 \mu\text{m}^{-1}$, $k_y = -0.852 \mu\text{m}^{-1}$, $k_y = 0 \mu\text{m}^{-1}$, $k_y = 0.852 \mu\text{m}^{-1}$, and $k_y = 1.677 \mu\text{m}^{-1}$. There are four modes along the transverse electric (TE) SLRs at energies of $E = 1.419$ eV ($k_y = -0.387 \mu\text{m}^{-1}$ and $k_y = 0.392 \mu\text{m}^{-1}$) and $E = 1.417$ eV ($k_y = -0.370 \mu\text{m}^{-1}$ and $k_y = 0.366 \mu\text{m}^{-1}$). For clarity, only the threshold curves for the modes at the slightly higher energy are shown in Figure 1c, and the other modes are shown in the Supporting Information, Figure S2. At energies of $E = 1.416$ eV are two peaks visible at $k_y = -1.281 \mu\text{m}^{-1}$ and $k_y = 1.279 \mu\text{m}^{-1}$. Lastly, there are two lasing peaks at $k_y = -2.046 \mu\text{m}^{-1}$ and $k_y = 2.050 \mu\text{m}^{-1}$ at an energy of $E = 1.400$ eV. Note that only the four lasing peaks that lie on the TE modes of the SLRs coincide with modes that can be seen in Figure 1b, whereas none of the modes at other lasing peaks are visible in the transmission measurement. The pump-dependent lasing spectra, the linewidths of the modes, and the divergence angles as a function of pump fluence are shown in the Supporting Information in Figures S3, S4, and S5, respectively. The quality (Q)-factors obtained by dividing the lasing energy by the FWHM of the lasing modes range for $E = 1.400$ eV from 933 to 2800, for $E = 1.416$ eV from 1200 to 1609, for $E = 1.417$ eV from 1610 to 1012, for $E = 1.419$ eV from 709 to 1419, and for $E = 1.428$ eV from 1298 to 1586. The Q-factors are in line with previously reported Q-factors of lasing in plasmonic arrays. The lasing thresholds and the intensities of the different lasing modes are clearly different, hinting that the modes are competing for the energy present in the system. However, as none of the modes lose intensity or disappear, we observe simultaneous lasing.

Figure 2 shows the dye emission with the lasing mode energies indicated. All of these modes coincide with the emission maximum. Interestingly, the Γ -point of the underlying square lattice ($E = 1.37$ eV) is located at an energy where no lasing takes place. This suggests that the modes originating from the supercell experience more gain or have lower losses and are therefore more likely to lase. By changing the square lattice period, we can conveniently shift the dispersions of the arrays with respect to the emission maximum of the dye. As a consequence, the modes that exhibit lasing can be tuned as shown in Figure S6 in the Supporting Information. Figure 2 shows that the lasing modes of the arrays with different periods overlap closely with the emission maximum of the dye.

RESULTS AND DISCUSSION

In Figure 3 the real space pattern of the nanoparticle array is shown in (a) along with its geometric structure factor $S(\mathbf{k})$ (b). The structure factor describes the scattering properties of the lattice for any given wave vector \mathbf{k} and can be interpreted as a measure of constructive interference along that scattering direction. In a typical square lattice, $S(\mathbf{k})$ has peaks of equal magnitude at reciprocal lattice sites, i.e., at the centers of the

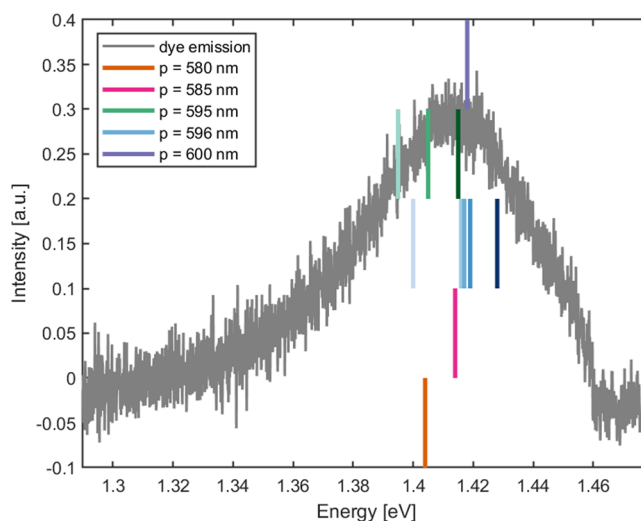


Figure 2. Emission spectrum of the dye (IR 140, 10 mM) pumped with a pump fluence of 1.259 mJ/cm². The lasing peak energies of the arrays with different periods $p = 580$, 585, 595, 596, and 600 nm are indicated, respectively, in orange, pink, green, blue, and purple, or from bottom to top with increasing period. They clearly overlap with the emission maximum, explaining why these modes are lasing.

Brillouin Zone (BZ). Removing particles from the array removes some of the destructive interference in the system allowing for new scattering directions to occur. The amplitude of these new scatterings depends on the number and positions of the particles removed. If particles are removed periodically, the system becomes periodic with a supercell period and has a new, smaller BZ. However, these new BZ:s are not made equal as their properties are dependent on the way particles are removed. Let us denote the initial square lattice period and the supercell period as p and q respectively, with associated reciprocal lattice vectors of magnitude a and b . For a periodic structure with a multiparticle unit cell, the normalized structure factor is

$$S(\mathbf{k}) = \frac{1}{N^2} \sum_{ij} e^{i\mathbf{k}\cdot(\mathbf{r}_i - \mathbf{r}_j)} = \frac{1}{N_u^2} \sum_{i'j'} e^{i\mathbf{k}\cdot(\mathbf{r}_{i'} - \mathbf{r}_{j'})} \cdot \frac{1}{N_\alpha^2} \sum_{\alpha\beta} e^{i\mathbf{k}\cdot(\mathbf{q}_\alpha - \mathbf{q}_\beta)} \frac{1}{\delta(\mathbf{k} - m_1\mathbf{b}_1 - m_2\mathbf{b}_2)} \quad (1)$$

where N_u and N_α are the number of particles in a unit cell and the number of unit cells, i, j and i', j' are the indices of the particles in the lattice and in a unit cell, \mathbf{q}_α and \mathbf{q}_β are the positions of unit cells, \mathbf{b}_1 and \mathbf{b}_2 are the reciprocal lattice vectors, and m_1 and m_2 are integers. As can be seen in Figure 3b, the system retains information from both periods. In addition to the original scattering peaks (yellow dots at the Γ -points of the square lattice), a new set of secondary peaks appears at the Γ -points of the supercell lattice, the strongest of which exist near the corners of the initial BZ. The new system retains information from the original period p as the $S(\mathbf{k})$ can be seen to repeat with a period of $a = 2\pi/p$.

The first approximation for the band-structure is given by the empty-lattice approximation (ELA), which is obtained by taking the convolution of geometric structure factor $S(\mathbf{k})$ with the in-plane free-photon dispersion $|\mathbf{k}| = \sqrt{k_x^2 + k_y^2} = nE/(\hbar c)$:³⁴ $\int d\mathbf{q} S(\mathbf{q}) \delta(|\mathbf{q} - \mathbf{k}| - nE/(\hbar c))$. This corresponds to placing light cones at the peaks of the structure factor (in the case of square (super) lattices, the Γ -points of each Brillouin zone) and weighing them by the value of the structure factor. This procedure is superior to the simple geometric ELA as it considers the structure of the unit cell and helps identify which

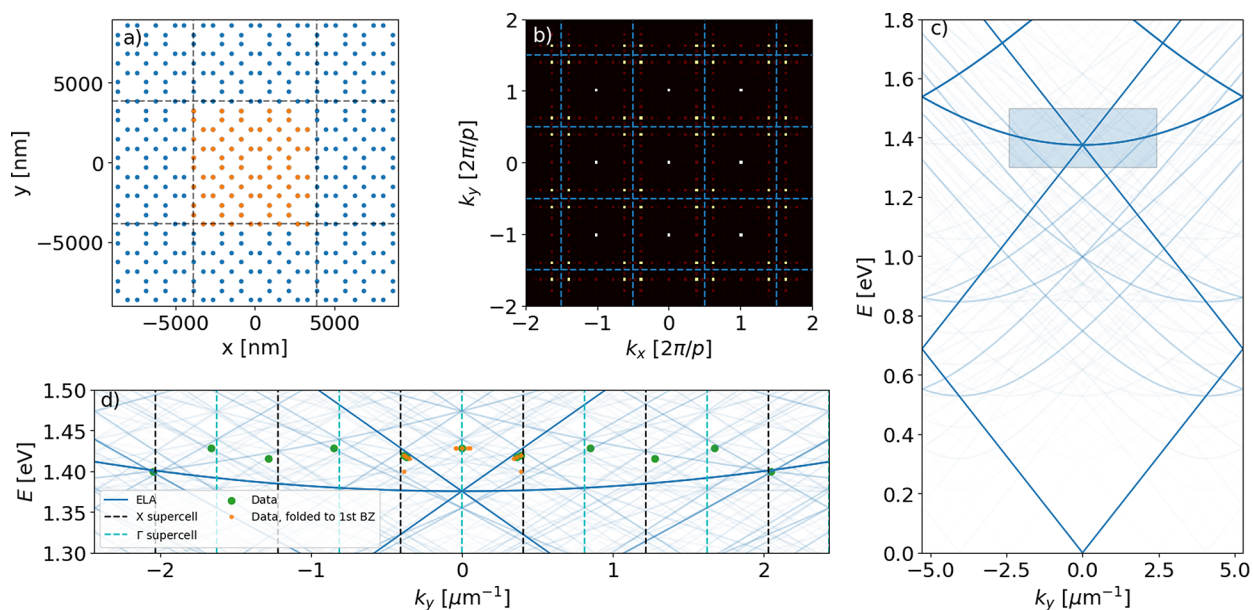


Figure 3. (a) Schematic picture of the lattice with the unit cell (orange) and superlattice period highlighted. (b) Structure factor calculated with eq 1 with dashed lines marking the reciprocal lattice as defined by the underlying square lattice. For clarity, the values shown are limited to $[0, 0.165]$. A close-up is shown in Figure S8. (c) Weighed empty-lattice approximation calculated from the structure factor. Line color correlates with the ELA weight. (d) Close-up of the dispersion relation close to the experimentally measured region (shaded area in c). The weights have been increased to make the fine structure more visible. Measured lasing peaks (green dots) are found to exist at crossings of at least two bands. When folded into the first BZ as defined by the superlattice (orange dots) period, we find that lasing peaks at the same energy actually correspond to the same high-symmetry point. For visual clarity the Γ and X-points of the supercell BZ have been highlighted in cyan and black dashed lines.

modes are strong and thus more likely to lase. The results are shown in Figure 3c. As $S(\mathbf{k})$ indicates the amount of constructive interference, the weight of the light-cone correlates with the strength of the mode. In addition to the typical ELA dispersions of a square lattice, additional weaker dispersions emerge from the Γ -points of the supercell. The experimentally measured dispersion overlaid with the calculated ELA is shown in Figure S7 in the Supporting Information showing a good agreement with the theoretical model and measurements. By comparing the measurements to the ELA dispersions, we find that the lasing peaks exist slightly below crossings of two or more bands at the high-symmetry points of the new BZ, as is shown in Figure 3d. Due to the large size of the supercell, the new BZ is small and can be repeated multiple times in the measured range. The modes at equal energy are separated by a multiple of $k_y = b$, so when folded back to the first BZ they can be seen to correspond to the same high-symmetry points. It is unclear whether in the experiments there exist even more lasing peaks at the same energy, as we are limited in k_y by the optics, i.e., the numerical aperture of the objective (see Supporting Information, Figure S1).

In order to verify that the lasing modes are the Γ - and X-points, we take cross-sections through the ELA in the k_x - k_y plane at specific energies, as shown in Figure 4. Note that in the experiments there is a small shift in the refractive index due to the dye molecules leading to a small shift in the energies of the crossings in the ELA and the observed lasing energies. The crosscuts show the weighted ELA in the first BZ of the underlying square lattices for energies $E = 1.434$ eV (Figure 4b), $E = 1.420$ eV (Figure 4c), and $E = 1.396$ eV (Figure 4d). The zoomed-in images show the experimentally relevant region around $k_x = 0$ spanning five BZ of the supercell in k_y . The supercell Γ - and X-points are indicated. We observe crossings of the ELA at different Γ - and X-points at different energies, namely, at Γ_{0-4} for $E = 1.434$ eV (Figure 4b), at $\Gamma_{1,3}$ and X_{0-5} for

$E = 1.420$ eV (Figure 4c), and at $X_{0,5}$ for $E = 1.396$ eV (Figure 4d). These crossings coincide with the lasing peaks observed in the experiments, identifying the lasing modes. We identify the lasing modes to be the 74th Γ -point and the 106th X-point if all modes are considered. The modes are counted from a standard ELA with the period of the superlattice.

Interestingly, some of the bands in the band structure in Figures 3c,d have different slopes than the TE and TM modes originating from the underlying square lattice (the lines with the highest weight). These modes with different slopes cannot be categorized as purely transverse electric/magnetic (TE/TM) modes, and the modes observed in the measurements coincide with such bands. This implies that the lasing modes are not purely TE or TM polarized.

To verify the hybrid TE/TM nature of the lasing states, we experimentally studied an array with the same lattice parameters ($p = 596$ nm and $q = 13p$), however, the edge length is now 240 μm . We combined the nanoparticle array with a reservoir of dye molecules with the same concentration of 10 mM as in the previous measurements, leading to an increased total amount of molecules. The larger array as well as the increased gain caused by the higher amount of molecules leads to a stronger signal. This is needed as we added a polarizer into the detection path, which decreases the amount of measurable light. We collected angle-resolved spectra as well as full momentum space images as is shown in Figure 5. Here, a vertical orientation refers to the axis of the polarizer oriented parallel to $k_x = 0^\circ$ and a horizontal orientation to the axis of the polarizer oriented parallel to $k_y = 0^\circ$.

Changing the size of the array changes the lasing spectrum. In total, five lasing peaks are clearly observable in Figure 5a, with an additional four peaks with less intensity. The peaks at the higher energy ($E = 1.403$ eV) are at wavevectors $k_y = -1.680, -0.859, 0, 0.845$, and $1.661 \mu\text{m}^{-1}$, which correspond directly to the wavevectors of the highest energy mode ($E = 1.428$ eV) of the

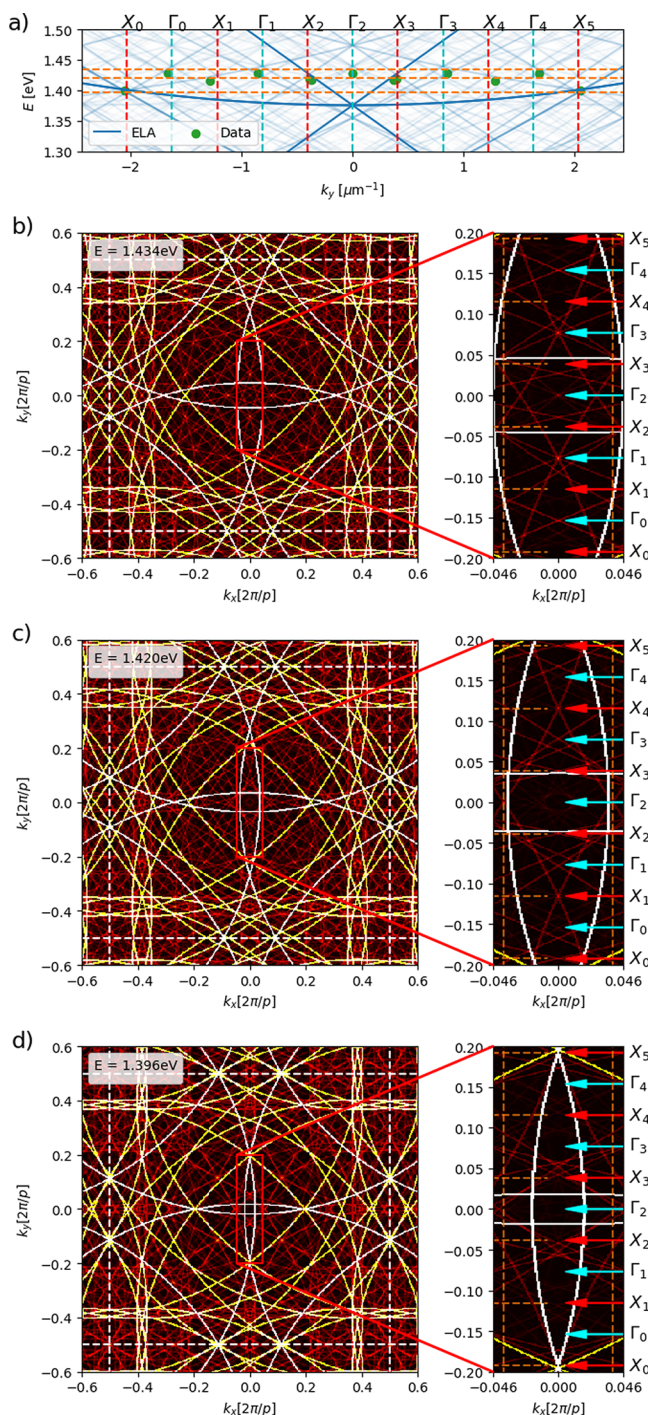


Figure 4. (a) Weighted empty lattice approximation calculated from the structure factor with the Γ and X points of the supercell indicated as vertical blue and red dashed lines, respectively. The horizontal orange dashed lines indicate three lasing energies where cross cuts through the k_x - k_y - E space are taken for lasing mode identification in (b)–(d), including a zoom-in showing the experimentally measured region. The white dashed lines in the left figures indicate the BZ boundaries of the underlying square lattice and the orange dashed lines in the right figures indicate the BZ boundaries of the supercell. (b) Cross-cut in the first BZ of the underlying square lattice for an energy of 1.434 eV. The zoom-in shows that there are crossings of different dispersions at the $\Gamma_{0,1,2,3,4}$ points, coinciding with the lasing peaks. (c) Cross-cut at $E = 1.420$ eV, where the zoom-in shows crossings at the $\Gamma_{1,3}$ - and X_{0-5} -points. (d) Cross-cut at $E = 1.396$ eV, with the zoom-in showing crossings at the $X_{0,5}$ -points.

smaller array shown in Figure 1c, and based on the weights of the ELA, we conclude that the lasing mode is now the 71st Γ -point. The size of the array has an influence on the quality factors of the modes: with increasing size, more nanoparticles scatter the light, leading to multiple scattering of the light. In each scattering event, the particles absorb light due to Ohmic losses, and hence change the quality factors of the modes.⁴³ The peaks at the lower energy in Figure 5a ($E = 1.393$ eV) occur at wavevectors -2.047 , -0.443 , 0.431 , and $2.024 \mu\text{m}^{-1}$, where the larger k_y directly correspond to the X -point lasing peaks in Figure 1c. The peaks at the smaller k_y are the X -points closest to k_y in Figure 3d. The shift in energy is most likely caused by the increased number of dye molecules that leads to a shift in the refractive index.

The majority of these peaks are visible in the angle-resolved spectra with polarization filters applied, albeit with varying intensity. Further, the peaks at $k_y = \pm 0.8 \mu\text{m}^{-1}$ and $E = 1.403$ eV do not appear in the case where a horizontally oriented polarizer is applied (Figure 5b), implying that these modes are TM polarized.

The full momentum space images in Figure 5, bottom row, show strong features along $\theta_{y/x} = 0^\circ$ if a horizontally/vertically oriented polarizer is applied. These images are on the logarithmic scale to make weaker features more visible. And indeed, although a polarizer is applied, the peaks along $\theta_{x/y} = 0^\circ$ can still be distinguished with a horizontal/vertical polarization filter applied. Nevertheless, these peaks are much weaker in intensity than the others, and although this implies the hybrid TE/TM nature of the modes, the modes are mainly TE or TM polarized.

For comparison, we simulated a superlattice-type version of our structure and found the results of such calculation to be in agreement with,²⁸ as is shown in Supporting Information, S9. Since both structures have the same supercell periodicity, band crossings happen at the same values of k and E . However, due to the differences in structure factors, these crossings have different weights, and thus, different bands are expected to be responsible for lasing. The strongest secondary bands in the supercell lattice exist in the vicinity of the original square lattice modes, while in our case the strongest secondary bands are found closer to the M -points. In this case, the observed crossings are not the results of these stronger bands, as is evident in Figure 3c,d. Instead, we find the crossings to come from multiple colliding weak modes. While these modes exist for the superlattice structure as well, the relative weights of the modes can be estimated to be different, as shown by the different weights of the lines in Figure 3 and Supporting Information, S9. In fact, the relative strengths of these crossings can be seen to correlate with the mode brightness.

CONCLUSION

We demonstrated multimode lasing in a plasmonic supercell lattice. We showed that by introducing a periodic supercell in a square lattice geometry, additional band edges are formed near high symmetry points of the supercell. These band edges enable lasing, and we observed lasing in multiple modes. By calculating the empty lattice approximation based on the structure factor of the lattice design, we identified the lasing modes to be the 74th Γ - and 106th X -point of the supercell. Due to their higher order nature, these lasing modes are not purely TE or TM polarized. By tuning the square lattice period with respect to the emission maximum of the gain medium, we were able to select the lasing modes. One advantage of the supercell approach compared to the superlattice approach is the relative size of the structure. In

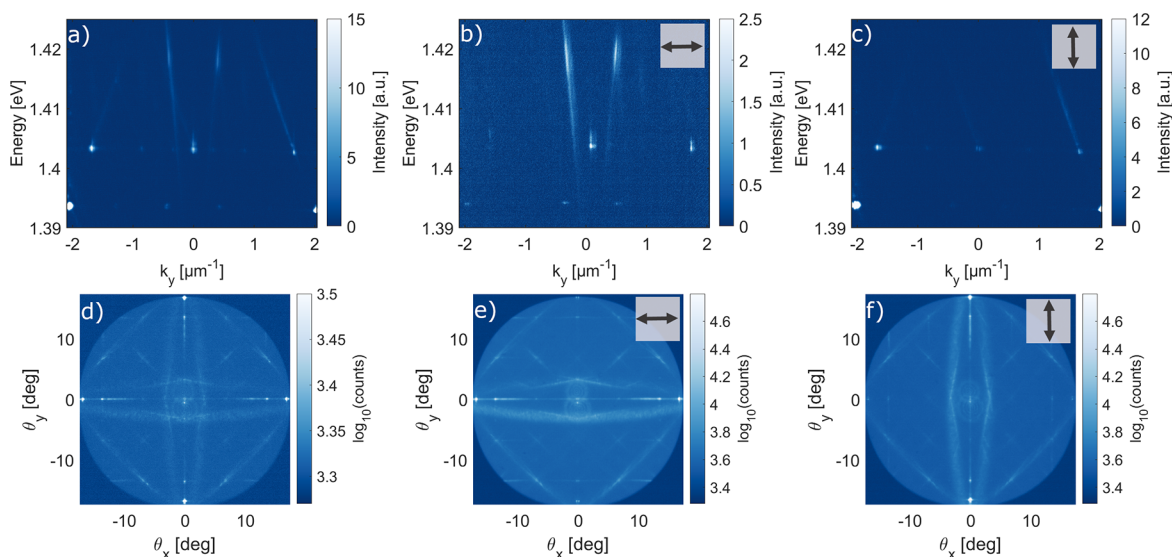


Figure 5. Polarization characteristics of the lasing modes in a large supercell array. The square lattice period is $p = 596$ nm and the edge length of the array is $240 \mu\text{m}$. Angle-resolved spectra for (a) no polarizer applied, (b) horizontally, and (c) vertically oriented polarizer. Full momentum space images in logarithmic scale for (d) no polarizer applied, (e) horizontally, and (f) vertically oriented polarizer.

previous superlattices in which multimode lasing has been achieved, the individual arrays of the size of 10s of μm were arranged on a centimeter square (10^{-4} m) scale.²⁸ The supercell arrays presented in this work, on the other hand, provide multimode in arrays with a size of $115 \mu\text{m} \times 115 \mu\text{m}$ (10^{-8} m) and are therefore significantly smaller.

The supercell design goes beyond state of the art complex array structures and is clearly different from, for instance, deterministic aperiodic structures based on mathematical sequences such as the Fibonacci or Thue-Morse sequence. One advantage over such structures is that the supercell size and particle distribution can be designed freely, offering more degrees of freedom. In the following, we will provide a few design principles of supercell arrays: The separation of the modes in k -space is controlled by the supercell period, which is different from the period of the underlying lattice. Making the size of the supercell larger will decrease the size of the Brillouin zone, moving the modes (light cones) closer together: this increases the number of crossings of different modes within a certain momentum interval. As the crossings are the points that can provide feedback for lasing, the supercell size can thus be used for controlling the k -values where lasing occurs. The underlying lattice period on the other hand shifts the band structure in energy. By matching the band structure with the emission wavelength of emitters, specific modes can be chosen for lasing. We also observed a connection between the relative brightness of the modes and the ELA-weight at the corresponding crossing. The exact distribution of the mode brightness depends on the structure factor, which again depends on the geometrical distribution of the particles in the supercell. By rearranging the particles in the supercell, the structure factor and hence the weight of the modes can be designed. We demonstrated this by comparing the here introduced supercell geometry with a previously studied superlattice geometry: the two clearly showed different ELA-weights. Hence, the relative weights can be tuned by the supercell geometry; this is also one advantage over the usual superlattice concept where the supercell is periodic and thus not freely tunable. We believe the inverse design process should be possible as well: this would

require reconstructing the lattice from a structure factor with desired properties.

■ ASSOCIATED CONTENT

Supporting Information

The Supporting Information is available free of charge at <https://pubs.acs.org/doi/10.1021/acsphotonics.3c00761>.

Experimental methods; Threshold curves of lower TE SLR lasing modes; Pump-dependent lasing spectra of the lasing modes; Pump-dependent line width of the lasing modes; Pump-dependent divergence angle of the lasing modes; Lasing experiments with different lattice periods; Measured dispersion and calculated ELA; Close-up of the structure factor; ELA of a superlattice (PDF)

■ AUTHOR INFORMATION

Corresponding Author

Päivi Törmä – Department of Applied Physics, Aalto University School of Science, FI-00076 Aalto, Finland; orcid.org/0000-0003-0979-9894; Email: paivi.torma@aalto.fi

Authors

Rebecca Heilmann – Department of Applied Physics, Aalto University School of Science, FI-00076 Aalto, Finland; orcid.org/0000-0003-2716-2571

Kristian Arjas – Department of Applied Physics, Aalto University School of Science, FI-00076 Aalto, Finland

Tommi K. Hakala – Center for Photonics Sciences, University of Eastern Finland, FI-80101 Joensuu, Finland

Complete contact information is available at:

<https://pubs.acs.org/10.1021/acsphotonics.3c00761>

Author Contributions

R.H. initiated the project and P.T. supervised it. R.H. fabricated the samples and performed the measurements. K.A. calculated the band structures. All authors discussed the results. R.H. and T.K.H. wrote the manuscript with input from all coauthors.

Funding

This work was supported by the Academy of Finland under Project No. 318937 (PROFI), 322002, the Academy of Finland Flagship Programme, Photonics Research and Innovation (PREIN), Project Nos. 320166 and 320167, and the Vilho, Yrjö and Kalle Väisälä Foundation. Part of the research was performed at the OtaNano Nanofab cleanroom (Micronova Nanofabrication Centre), supported by Aalto University. We acknowledge the computational resources provided by the Aalto Science-IT project. R.H. acknowledges financial support by the Finnish Foundation for Technology Promotion.

Notes

The authors declare no competing financial interest.

ACKNOWLEDGMENTS

We thank Grazia Salerno for valuable discussions on the calculation of the band structure based on the structure factor.

REFERENCES

- (1) Kravets, V. G.; Schedin, F.; Grigorenko, A. N. Extremely narrow plasmon resonances based on diffraction coupling of localized plasmons in arrays of metallic nanoparticles. *Phys. Rev. Lett.* **2008**, *101* (8), 087403.
- (2) Chu, Y.; Schonbrun, E.; Yang, T.; Crozier, K. B. Experimental observation of narrow surface plasmon resonances in gold nanoparticle arrays. *Appl. Phys. Lett.* **2008**, *93* (18), 181108.
- (3) Auguie, B.; Barnes, W. L. Collective resonances in gold nanoparticle arrays. *Phys. Rev. Lett.* **2008**, *101* (14), 143902.
- (4) Giannini, V.; Fernandez-Dominguez, A. I.; Heck, S. C.; Maier, S. A. Plasmonic nanoantennas: fundamentals and their use in controlling the radiative properties of nanoemitters. *Chem. Rev.* **2011**, *111* (6), 3888–3912.
- (5) Rodriguez, S. R. K.; Abass, A.; Maes, B.; Janssen, O. T. A.; Vecchi, G.; Gomez Rivas, J. Coupling bright and dark plasmonic lattice resonances. *Physical Review X* **2011**, *1* (2), 021019.
- (6) Humphrey, A. D.; Barnes, W. L. Plasmonic surface lattice resonances on arrays of different lattice symmetry. *Phys. Rev. B* **2014**, *90* (7), 075404.
- (7) Ross, M. B.; Mirkin, C. A.; Schatz, G. C. Optical properties of one-, two-, and three-dimensional arrays of plasmonic nanostructures. *J. Phys. Chem. C* **2016**, *120* (2), 816–830.
- (8) Väkeväinen, A. I.; Moerland, R. J.; Rekola, H. T.; Eskelinen, A.-P.; Martikainen, J.-P.; Kim, D.-H.; Törmä, P. Plasmonic surface lattice resonances at the strong coupling regime. *Nano Lett.* **2014**, *14* (4), 1721–1727.
- (9) Bozhevolnyi, S. I.; Martin-Moreno, L.; Garcia-Vidal, F. *Quantum Plasmonics*; Springer, 2017.
- (10) Hakala, T. K.; Moilanen, A. J.; Vakevainen, A. I.; Guo, R.; Martikainen, J.-P.; Daskalakis, K. S.; Rekola, H. T.; Julku, A.; Torma, P. Bose–einstein condensation in a plasmonic lattice. *Nat. Phys.* **2018**, *14* (7), 739–744.
- (11) De Giorgi, M.; Ramezani, M.; Todisco, F.; Halpin, A.; Caputo, D.; Fieramosca, A.; Gomez-Rivas, J.; Sanvitto, D. Interaction and coherence of a plasmon–exciton polariton condensate. *ACS Photonics* **2018**, *5* (9), 3666–3672.
- (12) Wang, W.; Ramezani, M.; Vakevainen, A. I.; Torma, P.; Rivas, J. G.; Odom, T. W. The rich photonic world of plasmonic nanoparticle arrays. *Mater. Today* **2018**, *21* (3), 303–314.
- (13) Vakevainen, A. I.; Moilanen, A. J.; Necada, M.; Hakala, T. K.; Daskalakis, K. S.; Torma, P. Sub-picosecond thermalization dynamics in condensation of strongly coupled lattice plasmons. *Nat. Commun.* **2020**, *11* (1), 3139.
- (14) Zhou, W.; Dridi, M.; Suh, J. Y.; Kim, C. H.; Co, D. T.; Wasielewski, M. R.; Schatz, G. C.; Odom, T. W. Lasing action in strongly coupled plasmonic nanocavity arrays. *Nat. Nanotechnol.* **2013**, *8* (7), 506–511.
- (15) Schokker, A. H.; Koenderink, A. F. Lasing at the band edges of plasmonic lattices. *Phys. Rev. B* **2014**, *90* (15), 155452.
- (16) Yang, A.; Hoang, T. B.; Dridi, M.; Deeb, C.; Mikkelsen, M. H.; Schatz, G. C.; Odom, T. W. Real-time tunable lasing from plasmonic nanocavity arrays. *Nat. Commun.* **2015**, *6* (1), 6939.
- (17) Ramezani, M.; Halpin, A.; Fernandez-Dominguez, A. I.; Feist, J.; Rodriguez, S. R.-K.; Garcia-Vidal, F. J.; Gomez Rivas, J. Plasmon-exciton-polariton lasing. *Optica* **2017**, *4* (1), 31–37.
- (18) Guo, R.; Necada, M.; Hakala, T. K.; Vakevainen, A. I.; Torma, P. Lasing at k points of a honeycomb plasmonic lattice. *Phys. Rev. Lett.* **2019**, *122* (1), 013901.
- (19) Juarez, X. G.; Li, R.; Guan, J.; Reese, T.; Schaller, R. D.; Odom, T. W. M-point lasing in hexagonal and honeycomb plasmonic lattices. *ACS Photonics* **2022**, *9* (1), 52–58.
- (20) Heilmann, R.; Salerno, G.; Cuerda, J.; Hakala, T. K.; Torma, P. Quasi-BIC mode lasing in a quadrumer plasmonic lattice. *ACS Photonics* **2022**, *9* (1), 224–232.
- (21) Mohamed, S.; Wang, J.; Rekola, H.; Heikkinen, J.; Asamoah, B.; Shi, L.; Hakala, T. K. Controlling topology and polarization state of lasing photonic bound states in continuum. *Laser & Photonics Reviews* **2022**, *16* (7), 2100574.
- (22) Salerno, G.; Heilmann, R.; Arjas, K.; Aronen, K.; Martikainen, J.-P.; Torma, P. Loss-driven topological transitions in lasing. *Phys. Rev. Lett.* **2022**, *129* (17), 173901.
- (23) Lu, Y.-J.; Wang, C.-Y.; Kim, J.; Chen, H.-Y.; Lu, M.-Y.; Chen, Y.-C.; Chang, W.-H.; Chen, L.-J.; Stockman, M. I.; Shih, C.-K.; Gwo, S.; et al. All-color plasmonic nanolasers with ultralow thresholds: autotuning mechanism for single-mode lasing. *Nano Lett.* **2014**, *14* (8), 4381–4388.
- (24) Liu, X.; Yi, S.; Zhou, X.; Zhang, S.; Fang, Z.; Qiu, Z.-J.; Hu, L.; Cong, C.; Zheng, L.; Liu, R.; Tian, P.; et al. Laser-based white-light source for high-speed underwater wireless optical communication and high-efficiency underwater solid-state lighting. *Opt. Express* **2018**, *26* (15), 19259–19274.
- (25) Zhao, J.; Yan, Y.; Gao, Z.; Du, Y.; Dong, H.; Yao, J.; Zhao, Y. S. Full-color laser displays based on organic printed microlaser arrays. *Nat. Commun.* **2019**, *10* (1), 870.
- (26) Guan, J.; Li, R.; Juarez, X. G.; Sample, A. D.; Wang, Y.; Schatz, G. C.; Odom, T. W. Plasmonic nanoparticle lattice devices for white-light lasing. *Adv. Mater.* **2023**, *35* (34), 2103262.
- (27) Wang, D.; Yang, A.; Hryn, A. J.; Schatz, G. C.; Odom, T. W. Superlattice plasmons in hierarchical Au nanoparticle arrays. *ACS Photonics* **2015**, *2* (12), 1789–1794.
- (28) Wang, D.; Yang, A.; Wang, W.; Hua, Y.; Schaller, R. D.; Schatz, G. C.; Odom, T. W. Band-edge engineering for controlled multi-modal nanolasing in plasmonic superlattices. *Nat. Nanotechnol.* **2017**, *12* (9), 889–894.
- (29) Wang, D.; Guan, J.; Hu, J.; Bourgeois, M. R.; Odom, T. W. Manipulating light–matter interactions in plasmonic nanoparticle lattices. *Acc. Chem. Res.* **2019**, *52* (11), 2997–3007.
- (30) Guo, K.; Kasture, S.; Koenderink, A. F. Plasmon antenna array “patchwork” lasers—towards low etendue, speckle free light sources. *OSA Continuum* **2019**, *2* (6), 1982–1997.
- (31) Cuartero-Gonzalez, A.; Sanders, S.; Zundel, L.; Fernandez-Dominguez, A. I.; Manjavacas, A. Super- and subradiant lattice resonances in bipartite nanoparticle arrays. *ACS Nano* **2020**, *14* (9), 11876–11887.
- (32) Lim, T.-L.; Vaddi, Y.; Bin-Alam, M. S.; Cheng, L.; Alaei, R.; Upham, J.; Huttunen, M. J.; Dolgaleva, K.; Reshef, O.; Boyd, R. W. Fourier-engineered plasmonic lattice resonances. *ACS Nano* **2022**, *16* (4), 5696–5703.
- (33) Zundel, L.; May, A.; Manjavacas, A. Lattice resonances induced by periodic vacancies in arrays of nanoparticles. *ACS Photonics* **2021**, *8* (1), 360–368.
- (34) Schokker, A. H.; Koenderink, A. F. Lasing in quasi-periodic and aperiodic plasmon lattices. *Optica* **2016**, *3* (7), 686–693.
- (35) Knudson, M. P.; Li, R.; Wang, D.; Wang, W.; Schaller, R. D.; Odom, T. W. Polarization-dependent lasing behavior from low-symmetry nanocavity arrays. *ACS Nano* **2019**, *13* (7), 7435–7441.

- (36) Guan, J.; Bourgeois, M. R.; Li, R.; Hu, J.; Schaller, R. D.; Schatz, G. C.; Odom, T. W. Identification of Brillouin Zones by in-plane lasing from light-cone surface lattice resonances. *ACS Nano* **2021**, *15* (3), 5567–5573.
- (37) Tan, M. J. H.; Park, J.-E.; Freire-Fernandez, F.; Guan, J.; Juarez, X. G.; Odom, T. W. Lasing action from quasi-propagating modes. *Adv. Mater.* **2022**, *34* (34), 2203999.
- (38) Lin, R.; Mazzone, V.; Alfaraj, N.; Liu, J.; Li, X.; Fratilocchi, A. On-chip hyperuniform lasers for controllable transitions in disordered systems. *Laser & Photonics Reviews* **2020**, *14* (2), 1800296.
- (39) Kim, H.-R.; Hwang, M.-S.; Smirnova, D.; Jeong, K.-Y.; Kivshar, Y.; Park, H.-G. Multipolar lasing modes from topological corner states. *Nat. Commun.* **2020**, *11* (1), 5758.
- (40) Gong, Y.; Wong, S.; Bennett, A. J.; Huffaker, D. L.; Oh, S. S. Topological insulator laser using valley-hall photonic crystals. *ACS Photonics* **2020**, *7* (8), 2089–2097.
- (41) Zhai, Z.; Li, Z.; Du, Y.; Gan, X.; He, L.; Zhang, X.; Zhou, Y.; Guan, J.; Cai, Y.; Ao, X. Multimode vortex lasing from dye–TiO₂ lattices via bound states in the continuum. *ACS Photonics* **2023**, *10* (2), 437–446.
- (42) Azzam, S. I.; Chaudhuri, K.; Lagutchev, A.; Jacob, Z.; Kim, Y. L.; Shalaev, V. M.; Boltasseva, A.; Kildishev, A. V. Single and multi-mode directional lasing from arrays of dielectric nanoresonators. *Laser & Photonics Reviews* **2021**, *15* (3), 2000411.
- (43) Nečada, M.; Törmä, P. Multiple-scattering T-matrix simulations for nanophotonics: Symmetries and periodic lattices. *Commun. Comput. Phys.* **2021**, *30* (2), 357–395.